Journal of Sol-Gel Science and Technology, 4, 117–133 (1995)

Structure-Property Relationships in Thin Films and Membranes

C.J. BRINKER
Ceramic Synthesis and Inorganic Chemistry Department 1846, M.S. 1349, Sandia National Laboratories, Albuquerque, NM 87185, and UNM/NSF Center for Micro-Engineered Ceramics, University of New Mexico, Albuquerque, NM 87131

N.K. RAMAN
UNM/NSF Center for Micro-Engineered Ceramics, University of New Mexico, Albuquerque, NM 87131

M.N. LOGAN
Ceramic Synthesis and Inorganic Chemistry Department 1846, M.S. 0607, Sandia National Laboratories, Albuquerque, NM 87185

R. SEHGAL
UNM/NSF Center for Micro-Engineered Ceramics, University of New Mexico, Albuquerque, NM 87131

R.-A. ASSINK
Properties of Organic Materials Department 1812, M.S. 0367, Sandia National Laboratories, Albuquerque, NM 87185

D.-W. HUA AND T.L. WARD
UNM/NSF Center for Micro-Engineered Ceramics, University of New Mexico, Albuquerque, NM 87131

Received November 16, 1992; accepted July 15, 1994

Abstract. The molecular-scale species distributions and intermediate-scale structure of silicate sols influence the microstructures of the corresponding thin films prepared by dip-coating. Using multi-step hydrolysis procedures, we find that, depending on the sequence and timing of the successive steps, the species distributions (determined by ^{29}Si NMR) and intermediate scale structure (determined by SAXS) can change remarkably for sols prepared with the same nominal composition. During film formation, these kinetic effects cause differences in the efficiency of packing of the silicate species, leading to thin film structures with different porosities.

Keywords: kinetics, precursor chemistry, silica, permeability, microstructure

1 Introduction

The ability to control the microstructural features of the deposited film (e.g. pore volume, pore size, and surface area) is an outstanding advantage of sol-gel processing over conventional thin film processing techniques. Our previous research (1) has documented that the thin film microstructure is established by evaporation-induced aggregation of sol species within the thinning film to form a physical or chemical gel and the subsequent collapse of the gel due to capillary forces exerted during the final stage of drying (see Fig. 1). The porosity of the film therefore depends on the porosity of the primary species—either polymers or particles—and that created or lost by the subsequent aggregation and drying processes associated with film deposition. In this paper we explore relationships between the size and structure of primary sol species as revealed by NMR and SAXS and the properties of the corresponding films as characterized by ellipsometry, TEM, and transport measurements. We limit our discussion to the deposition of silica sols where microstructural development can be qualitatively understood on the basis of fractal aggregation.

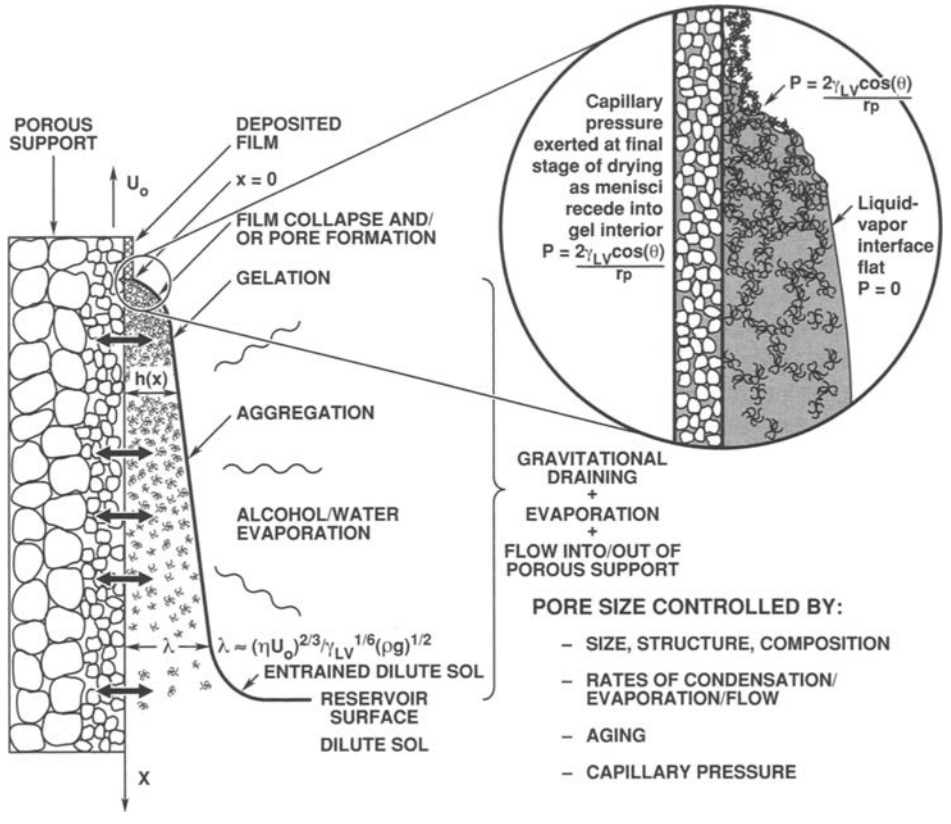

Fig. 1. Schematic of the steady state sol-gel dip-coating process on a porous support, showing the sequential stages of structural development that result from draining accompanied by solvent evaporation and continued condensation reactions. Inset shows the collapse of the gel network during the final stage of drying.

1.1 Aggregation of fractals

Under many conditions of silicate sol synthesis, the primary species are characterized by a mass fractal dimension D (2) that relates the polymer mass M to its radius r_c as:

$$M \propto r_c^D. \tag{1}$$

The porosity Π of an object varies inversely with density, so in three dimensional space:

$$\Pi \propto r_c^3/r_c^D \quad \text{or} \quad \Pi \propto r_c^{3-D}. \tag{2}$$

Thus, for mass fractals ($0 < D < 3$), the porosity of an individual object increases with its size, whereas for uniform objects ($D = 3$), porosity is invariant with size.

During film formation by dip-coating, primary sol species are rapidly aggregated by evaporation of solvent. The porosity of the secondary aggregate structure depends on the extent of interpenetration of the primary species. The extent of interpenetration is inversely related to the mean number of intersections $M_{1,2}$ of two polymers of radius r_c and mass fractal dimension $D1$ and $D2$ confined to the same region of three-dimensional space (2):

$$M_{1,2} \propto r_c^{D1+D2-3}. \tag{3}$$

From Eq. 3 we see that there are two classes of fractal polymeric sols. If the polymers exhibit fractal dimensions less than 1.5, the probability of polymer intersection decreases indefinitely with r_c. This situation should favor interpenetration of polymers within the thinning film during dip-coating. We refer to this class of sol species as *mutually transparent*, meaning that they move through one another freely. Alternatively, if the fractal dimension of each polymer exceeds 1.5, the probability of intersection increases algebraically with r_c. In this situation, polymer interpenetration is impeded (by points of intersection) as the polymers are

concentrated during dip-coating. We refer to this class of sol species as *mutually opaque*.

Equation 3 assumes every point of intersection results in immediate and irreversible attachment, chemically equivalent to an infinite condensation rate. Finite condensation rates mitigate the criterion for mutual transparency, i.e. since every point of intersection does not result in immediate and irreversible "condensation", interpenetration may occur for structures characterized by $D > 1.5$. The value of Eq. 3 is that it provides a qualitative understanding of the effect of structure on the extent of polymer interpenetration and thus porosity: smaller polymer sizes and lower mass fractal dimensions favor denser films, and larger polymer sizes and greater mass fractal dimensions favor more porous films. In all cases increased condensation rates reduce the tendency toward interpenetration, favoring more porous films.

1.2 Multi-step hydrolysis procedures

Two general multi-step procedures were used to prepare the precursor sols: a) a two-step acid-catalyzed hydrolysis of tetraethoxysilane (TEOS), using H_2O/Si molar ratio $r = 5$, or b) a two- or three-step acid/base-catalyzed hydrolysis of TEOS, using $r = 3.7$. Using multi-step hydrolysis procedures, it is possible to vary the sequence of the hydrolysis steps or the aging conditions between steps to obtain sols of the same nominal composition but with different species distributions and structures. Throughout this study we discovered examples of the role of such kinetic effects on the species distributions and structure of silicate sols. In many cases these effects are manifested in the properties of the corresponding films or membranes. We have confined our discussion to comparisons of sols (either acid- or acid/base-catalyzed) prepared with identical r values, pH and silica concentrations. The only differences are the sequence of the hydrolysis steps and the aging conditions. This comparison elucidates the role of kinetics in dictating the structures of silicate sols and the corresponding deposited films.

2 Experimental procedure

2.1 Sol preparation

A two-step acid-catalyzed process was used to prepare one series of silicate sols. In the first step tetraethoxysilane (TEOS), ethanol, H_2O and HCl were mixed in the molar ratio 1:3.8:1.1:0.0007, refluxed at 60°C for 90 min and cooled to room temperature (3). We refer to the silicate solution obtained after the first hydrolysis step as the *stock solution*. The stock solution was used immediately or stored in a freezer at 0°C. In the second hydrolysis step additional water and HCl were added at room temperature resulting in the final molar ratio of 1:3.8:5.1:0.056. The second hydrolysis step was performed on the stock solution after aging 0–7 days at 0°C or after aging 4–5 months at 0°C. These sols are identified as A2(fresh) and A2(aged), respectively. After stirring for 10 min, the A2 sols were allowed to age at 50°C for periods ranging from 2 to 35 hr and then diluted 2:1 with ethanol (vol EtOH:vol sol) prior to film deposition. Gelation times for the A2(fresh) and A2(aged) sols were determined at 50°C using undiluted A2 sols.

A two- or three-step acid/base-catalyzed process was used to prepare a second series of sols identified as B2 (4) or AAB (5), respectively. An aged (10 days to 8 months) stock solution was the starting point for both sols. For B2 the second hydrolysis step consisted of adding an aqueous solution of 0.05 M NH_4OH and diluting with ethanol, resulting in a final molar ratio of TEOS:EtOH:H_2O:HCl:NH_4OH of 1:48:3.7:0.0007:0.002, and a final sol pH of 5.5 as estimated using colorimetric pH indicator strips (EM Science). For AAB the second step consisted of adding 1M HCl diluted in ethanol, resulting in a H_2O/Si ratio $r = 2.5$, and refluxing at 60°C for 60 min. The third step consisted of adding an aqueous solution of 2M NH_4OH diluted in ethanol, resulting in a final molar ratio of 1:48:3.7:0.028:0.05. The AAB sols had the same final dilution, r value (3.7) and pH (5.5) as the B2 sols. The diluted sols were aged at room temperature or in a Class A (explosion-proof) oven at 50°C, and samples were removed at intervals up to the gel point or allowed to gel. The gelled samples were subjected to ultrasound to prepare sols of a consistency suitable for dip-coating.

2.2 ^{29}Si NMR investigations

^{29}Si NMR was employed to determine the species distribution of the stock solution and A2, B2, and AAB sols after various periods of aging. ^{29}Si NMR spectra were recorded at 39.6 MHz, on a Chemagnetics console interfaced to a General Electric 1280 data station and pulse programmer. Chromium(III) acetylacetonate (Cr(acac)3, 15.7 mM) was added as a paramagnetic relaxation agent. Twenty millimeter diameter quartz

sample tubes were used, which made negligible contributions to the baseline due to their very long spin relaxation times. Proton decoupling and a silicon free probe were employed during data acquisition (6).

2.3 *SAXS measurements*

The effects of synthesis and aging conditions on the intermediate-scale sol structure (0.5–30 nm) were determined by small angle x-ray scattering (SAXS). SAXS data were collected on liquid samples, using a Rigaku-SAXS setup having a Kratky U-slit system. The incident beam was Cu-Kα radiation with a wavelength of 1.542 Å. The data were corrected for slit collimation. The Guinier radius, R_G, and the mass fractal dimension, D, were calculated from the Guinier and Porod regions, respectively.

2.4 *Film formation*

For all sols, films were deposited on polished single crystal ⟨100⟩ silicon substrates by dip-coating in a dry nitrogen atmosphere, using substrate withdrawal rates of 20 (A2 and AAB sols) or 25 cm/min (B2 sols). A2 films were dried at room temperature and annealed at 400°C for 10 min using a heating rate of 10°C/min. B2 and AAB films were dried ~70°C for 20 min, using a heat lamp. Selected films were supported on edge in quartz trays and fired in air at 400°C for 10 min with an estimated 50°C/min ramp achieved by placing the quartz trays directly on ZrO_2 tiles maintained at the firing temperature.

The A2 series of films were also prepared as supported membranes by sol deposition on commercial (U.S. Filter) Membralox alumina supports. Approximately 5 cm sections of tubular supports were calcined at 400°C for 10 min and outgassed in He at 150°C for 8 hours prior to membrane deposition. Tubes were mounted on a linear translation stage in a dry box and dipped into the sol at a rate of 20 cm/min. After an immersion time of 100 s, supports were withdrawn at a rate of 20 cm/min and allowed to dry in a flowing dry N_2 ambient for 15 min. Deposited membranes were calcined in air at a rate of 1°C/min to 400°C, held at 400°C for 10 min and cooled to room temperature at 1°C/min. A more detailed description of the sol deposition process is given in a previous publication (7). The major difference between films deposited on solid substrates (Si) and porous supports is that liquid flow into the support deposits some material by slip-casting and protracts the film drying process (due to flow of liquid from the support into the drying film).

2.5 *Film characterization*

Refractive indices and thicknesses of films deposited on silicon substrates were determined by ellipsometry using either a Rudolph AutoEL IV or Gaertner Model L116-C ellipsometer and assuming an absorption coefficient of 0 at $\lambda = 632.8$ nm. The thickness and morphology of films prepared as membranes were evaluated by cross-sectional TEM (7).

2.6 *Transport measurements*

The permeabilities of the membranes were investigated using single gas (He, N_2, and C_3H_6) permeation measurements. A detailed description of the permeability equipment and technique used has been provided elsewhere (7). Briefly, the tubular membranes were sealed by viton gasket material in a permeation cell. Pure gases were flowed through the membrane, with the flow rate determined by a mass flow controller or mass flow meter. The pressure difference across the membrane corresponding to a particular permeation rate was measured, leading to the calculated quantity that we call permeance (defined below). Prior to testing, membranes were outguessed at approximately 150°C for 8 hours under He flow and cooled to room temperature.

Permeation measurements were performed at room temperature as a function of average pressure across the membrane. Permeance is defined in terms of the flux (volumetric or molar) at standard temperature and pressure (STP) and the pressure difference across the membrane:

$$J(\text{cm}^3(\text{STP})/\text{cm}^2\text{-s}) = F_T \Delta P, \tag{4}$$

where F_T is the permeance of the membrane, ΔP is the total pressure difference across the membrane, and J is the gas permeation rate per unit area of membrane. Permeance data in this paper are reported in units of $\text{cm}^3(\text{STP})/(\text{cm}^2\text{-s-cm Hg})$. The commonly used unit for membrane "permeability", the Barrer (1 Barrer $= 10^{-10}$ $\text{cm}^3(\text{STP})\text{-cm}/(\text{cm}^2\text{-s-cm Hg})$), would be obtained by multiplying the permeance by the appropriate layer thickness. However, with composite membrane structures the transport resistance may have contributions from more than one layer, thus making the appropriate layer thickness for permeability calculation uncertain. For these types of membranes, permeance

is generally a more useful quantity. However, if one particular layer of the composite structure dominates the transport resistance, then permeance can be converted to conventional permeability by multiplying by that layer thickness.

2.7 *Thermal gravimetric analysis*

TGA experiments were performed on B2 and AAB xerogel powders dried at 50°C for 20.5 hours. Experiments were performed in flowing air (50 sccm) at a heating rate of 2°C/min to 550°C and 10°C/min to 1000°C.

3 Results

In this section we report the properties of the sols as determined by ^{29}Si NMR and SAXS and the properties of the corresponding films as deduced from ellipsometry and transport measurements. We use transport measurements in addition to ellipsometry to characterize the A2 series of films, because we observed little variation in the refractive index values of these samples but significant differences in permeance.

3.1 ^{29}*Si NMR*

The Q-notation (8) is used to identify the silicic acid ester structures. The basic structural unit is described as a Q-unit, a silicon bonded to four oxygen atoms. The superscript on the Q-unit represents the number of siloxane bonds (–OSi) attached to the silicon under consideration. The subscript 4c identifies the silicon as being contained in a cyclotetrasiloxane ring composed of 4 SiO_4^{4-} tetrahedra. The assignments for the Q^n resonances were made by comparison with literature data (9, 10).

Stock solution. Figures 2(a) and (b) show the ^{29}Si NMR spectra for the fresh and aged stock solutions along with the respective peak assignments. The most significant differences between the two spectra are the increased concentration of cyclic species, Q^2_{4c}(−95.5 ppm) and Q^3_{4c}(−103 ppm), and the decreased concentration of the hydrolyzed dimer species (−86.5 ppm) in the aged stock solution compared to the fresh stock solution. The aged stock solution also contains considerably more Q^3 species (−101 to −105 ppm) consistent with a greater overall extent of reaction. Both sols contain quite high concentrations of unhydrolyzed dimer (−89 ppm).

A2 sols. Figure 3 (a–d) shows the NMR spectra of the A2(fresh) and A2(aged) sols after 2 or 35 hours of aging at 50°C. The spectra have three broad peaks centered at −92, −101, and −110 ppm attributable to the highly varied environments of silicon contained in Q^2, Q^3, and Q^4 units, respectively. Figure 4 shows the distribution of the Q^n species as a function of aging time as determined by deconvolution of the corresponding ^{29}Si NMR spectra (e.g. Fig. 3). Although the A2(fresh) sol is clearly less highly condensed after 2 hours aging, the differences in overall extent of condensation largely vanish after 35 hours aging.

B2 and AAB sols. Figure 5 compares the spectra of an unaged B2 sol and a B2 sol aged 39 hours at 50°C. Although both spectra show broad features due to Q^3 and Q^4 silicon species, the spectra appear dominated by much sharper resonances associated mainly with monomers and weakly hydrolyzed Q^1 and Q^2 silicon species: in particular the unhydrolyzed monomer (−82.1 ppm), the unhydrolyzed dimer (−89.1 ppm), the unhydrolyzed cyclic tetramer Q^2_{4c}(−95.4 ppm), and an unhydrolyzed Q^2 species possibly associated with a trimer (−96.5 ppm). Figure 6 shows the evolution of the Q^n species distribution with aging time. We see that although the percent of Q^4 species increases at the expense of Q^2 and Q^3 species, consistent with further condensation, the percentage of Q^1 species remains virtually constant (30%), and the concentration of monomer increases from about 2 to 7%.

Figure 7(a) shows the ^{29}Si NMR spectrum of an AAB sol after the second hydrolysis step (r = 2.5, dilution = 2:1). We observe two broad peaks attributable to Q^2 and Q^3 species. There is no evidence of monomer or end groups/dimers consistent with a more extensive state of hydrolysis and condensation promoted by the additional acid-catalyzed hydrolysis step. Figure 7(b) shows the spectrum of an AAB sol (diluted 5:1) three hours after the third (base-catalyzed) hydrolysis step. Q^2, Q^3 and Q^4 species are present in the proportions 11%, 46% and 43%, respectively. Figure 7(c) shows the solid state magic angle spinning spectrum of an AAB gel. Q^3 and Q^4 species are present in the proportions 60% and 40%, respectively. It is clear from Figs. 7(a–c) that although AAB sols and gels have the same final pH and hydrolysis ratio r as the B2 sol, the Q^n species distribution is completely different: there

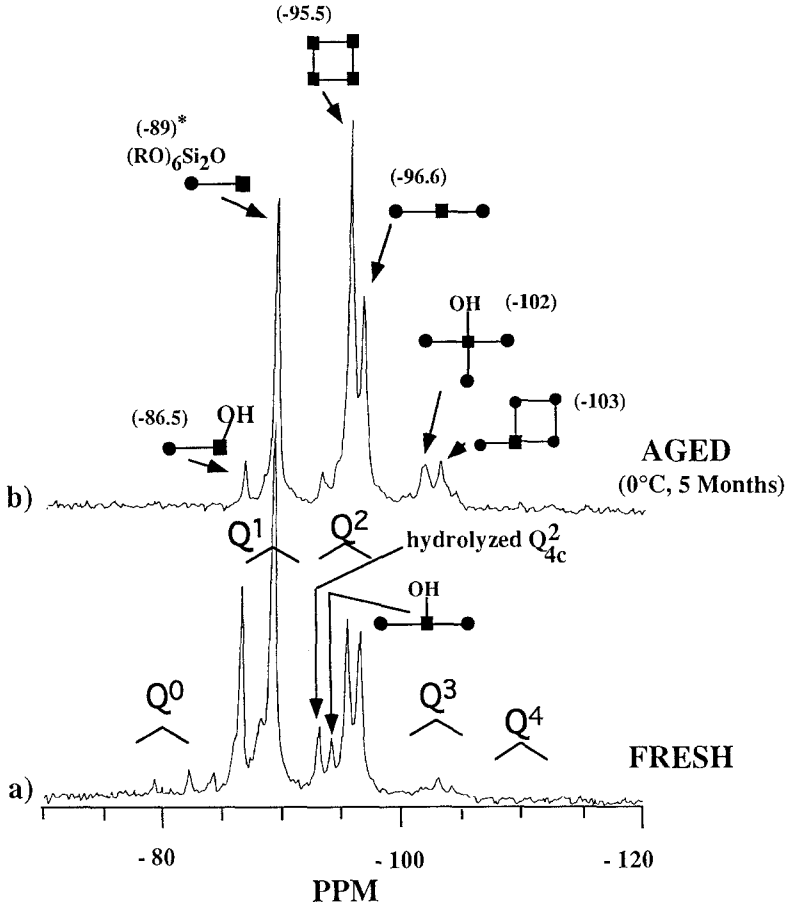

Fig. 2. ^{29}Si NMR spectra of: (a) the fresh stock solution and (b) the aged stock solution. Peak assignments are from reference (9). The squares represent the Si atom under consideration and circles represent all other Si atoms in the molecule. Alkoxy groups are implied where not shown to make the Si 4-coordinate, and oxygen atoms are assumed between all Si atoms. *High resolution studies indicate that the −89 ppm peak is attributable to over 75% unhydrolyzed dimer.

is no evidence of monomer or end groups/dimers even after extensive aging of the sol.

3.2 *Small angle X-ray scattering*

SAXS was employed to investigate the growth and structure of the silicate species before gelation. Figures 8(a) and (b) show the Porod plots (log scattered intensity vs log scattering wave vector, q) for A2(fresh) and A2(aged) sols after 2 or 35 hours aging at 50°C. For the A2(fresh) sols, limiting values of the Porod slopes (q values between about 0.15 and 0.3 Å^{-1}) suggest a limited range of fractal scaling with D increasing from about 1 to 1.7 over a period of 35 hours of aging. Above $q \approx 0.33$ Å^{-1}, all three curves exhibit Porod slopes of about -1.9. Guinier radii (R_G) evaluated at low q increase from 1.3 to 2.6 nm over the same time period. The A2(aged) sols exhibit power law scattering over a wider range of q than observed for the A2(fresh) sols. With aging, D increases from 1.18 to 1.4 and R_G increases from 2.0 to greater than 5.7 nm.

Figures 9(a) and (b) show Porod plots of B2 and AAB sols, respectively, after different periods of aging. For the B2 sol, Porod slopes evaluated over the q range 0.01 to 0.1 Å^{-1} suggest that the sol is composed of fractal clusters with D increasing from about 2.3 to 2.4 over a 48 hour period of aging. Although the crossover to the Guinier region of scattering is not clearly established for the sol aged 48 hours, compared to the sol aged 0 hours, it is displaced to lower q consistent with further polymer growth accompanying the aging process. Compared to the B2 sols, after comparable periods of aging, the AAB sols exhibit both power law scattering over a much greater q range and less negative values of the Porod slope. During 44 hours of

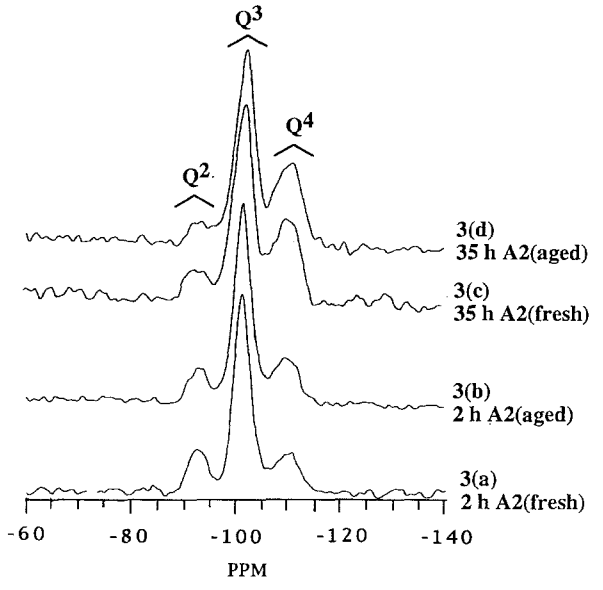

Fig. 3. ^{29}Si NMR spectra of: (a) the 2 hr aged A2(fresh) sol; (b) the 2 hr aged A2(aged) sol; (c) the 35 hr aged A2(fresh) sol; and (d) the 35 hr aged A2(aged) sol.

aging, D increases from about 1.4 to 1.7. Compared to B2 sols, the crossover to Guinier scattering apparently occurs at lower q, consistent with larger average cluster size.

3.3 Ellipsometry and thermal gravimetric analysis

Ellipsometry was performed on thin film samples deposited on silicon substrates to determine film thickness and refractive index. Table 1 lists values of thickness and refractive index for films prepared from A2(fresh) and A2(aged) sols after varying periods of aging (prior to film deposition) and annealing at 400°C. Volume fraction porosities were calculated from the refractive index using the Lorentz-Lorenz model assuming a skeletal refractive index of 1.45 for silica. We see that refractive index values are quite similar, corresponding to about 10% porosity, regardless of the pedigree of the sol or the aging times employed.

Table 2 lists refractive index and percent porosities for films prepared from B2 or AAB sols after various sol aging times (prior to film deposition). Whereas there is little effect of aging on the porosity of as-deposited (unannealed) B2 films, the as-deposited AAB films show a clear increase in porosity with aging time. For both B2 and AAB films, heating to 400°C causes a reduction in refractive index corresponding to an increase in porosity. After heating *both* AAB and B2 films exhibit an increase in porosity with aging time. Corresponding TGA results (Fig. 10) shows a much greater weight loss for B2 specimens than for AAB

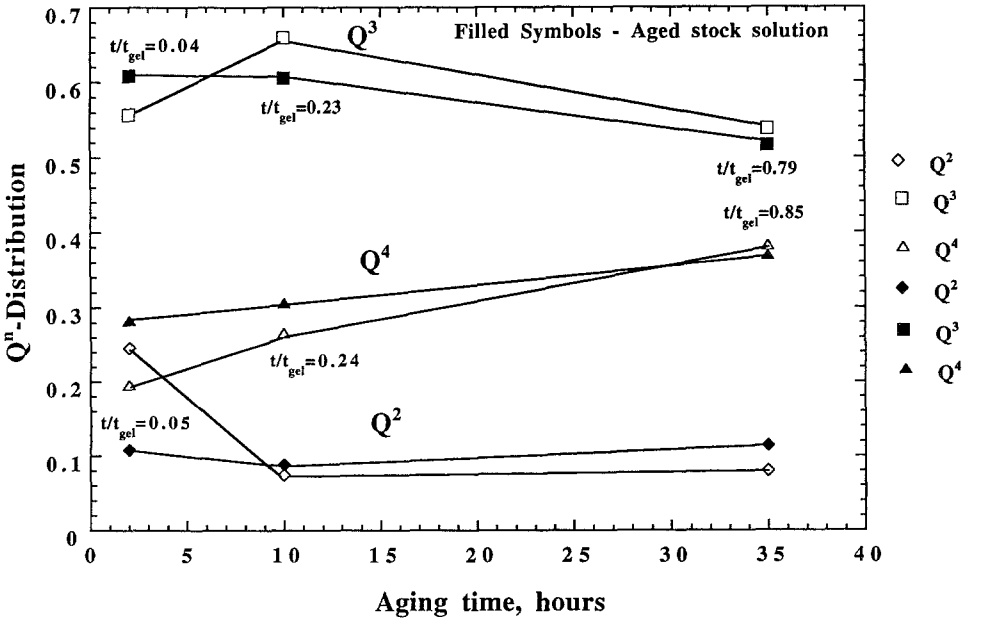

Fig. 4. Q^n distribution of the A2(fresh) and A2(aged) sols with aging time at 50°C. The lines are drawn to guide the eye. The gelation time of the A2(fresh) and A2(aged) sols at 50°C prior to dilution was 41 and 44 hours, respectively. Different t/t_{gel} values for the same aging times are due to different t_{gel} times.

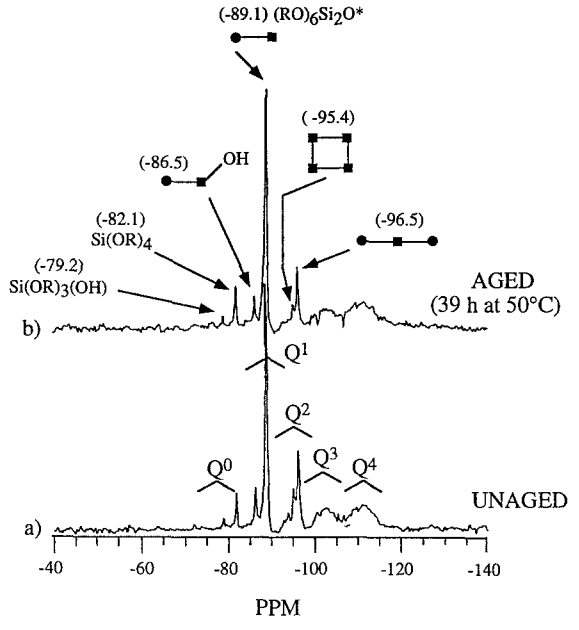

Fig. 5. ^{29}Si NMR spectra of B2 sols (diluted 4:1): (a) unaged and (b) aged 39 hours at 50°C. Peak assignments are from reference (9). The squares represent the Si atom under consideration and circles represent all other Si atoms in the molecule. Alkoxy groups are implied where not shown to make the Si 4-coordinate, and oxygen atoms are assumed between all Si atoms. *High resolution studies indicate that the −89 ppm peak is attributable to over 75% unhydrolyzed dimer.

specimens in the temperature range 150–130°C associated with pyrolysis of residual alkoxide groups.

3.4 Transport characterization

In order to obtain additional information concerning the porosity of the A2 series of films, which showed no dependence of refractive index on sol aging time, we prepared A2 films in supported membrane configurations and measured the permeance of several gases. Figure 11 shows cross-sectional TEM images of the supported membranes prepared from A2(aged) sols after various periods of aging. Figures 12 and 13 show plots of helium permeance versus average pressure across the membrane for bare supports and for supports coated with A2(fresh) or A2(aged) sols aged for 2 and 35 hours, respectively. The permeance of the support before and after membrane deposition was essentially independent of the mean pressure, indicating that the supports and membranes are free of large (viscous flow) defects.

For both fresh and aged stock sols and all aging times, the deposition of a single coating led to a substantial reduction in permeance. Considerable variability in the permeance of supports prior to coating was observed. This is believed to be due to variations in the thickness of the ~4 nm pore diameter γ-Al_2O_3 support layer. We have therefore evaluated the effect of membrane coating on permeance in terms of a normalized reduction in permeance, which we call the reduction ratio. The reduction ratio is the ratio of permeance

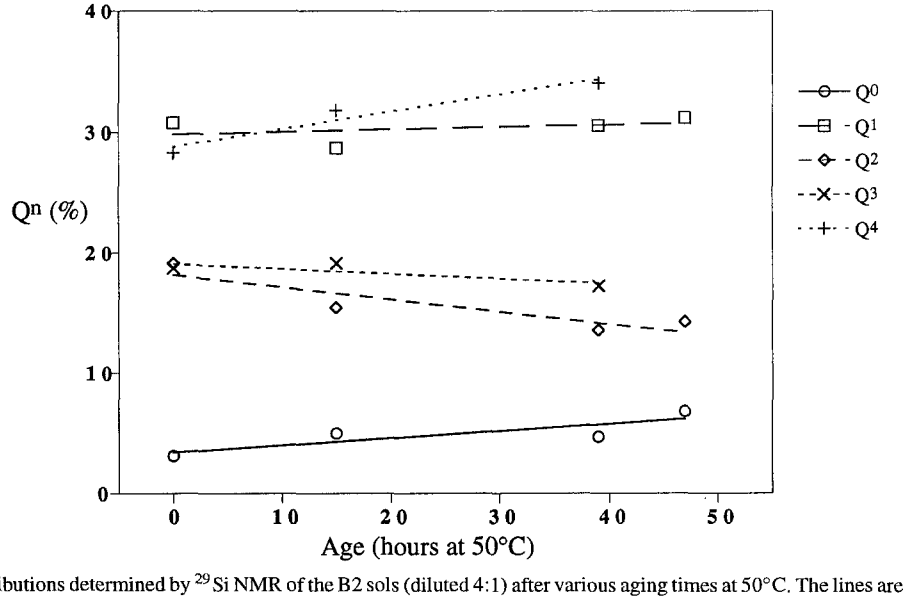

Fig. 6 Q^n distributions determined by ^{29}Si NMR of the B2 sols (diluted 4:1) after various aging times at 50°C. The lines are linear regressions of the data.

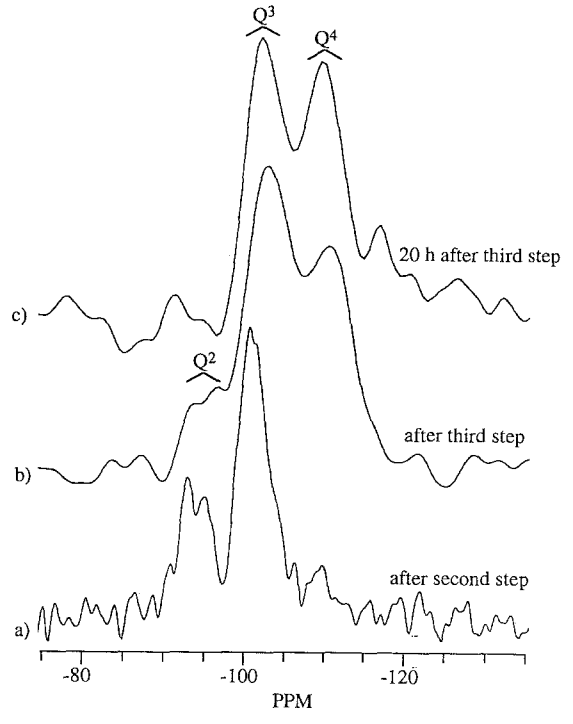

Fig. 7. ^{29}Si NMR spectra of the AAB sols: (a) after the second hydrolysis step, diluted 2:1 (b) 3 hours after the third hydrolysis step, diluted 5:1, and (c) magic angle spinning NMR spectrum of an AAB gel 20 hours after the third hydrolysis step.

of the support prior to coating to the permeance after depositing the membrane coating. The He permeance data along with the reduction ratios for supports coated with A2(fresh) and A2(aged) sols after different aging times are presented in Tables III(a) and (b). Nitrogen and C_3H_6 permeances were also measured for the membranes presented in Table III, and the reduction ratios exhibited trends similar to those found for He.

4 Discussion of sols

4.1 Stock solution

The stock solution is prepared by the acid-catalyzed hydrolysis of TEOS with sub-stoichiometric water ($r = 1$). ^{29}Si NMR studies of the fresh stock solution indicate that weakly-branched oligomeric species (Q^1 and Q^2) are the initial products of condensation. With aging, further condensation occurs, as is evident from the significant reduction in all hydrolyzed species and the appearance of branched (Q^3) species. Whereas the concentration of unhydrolyzed

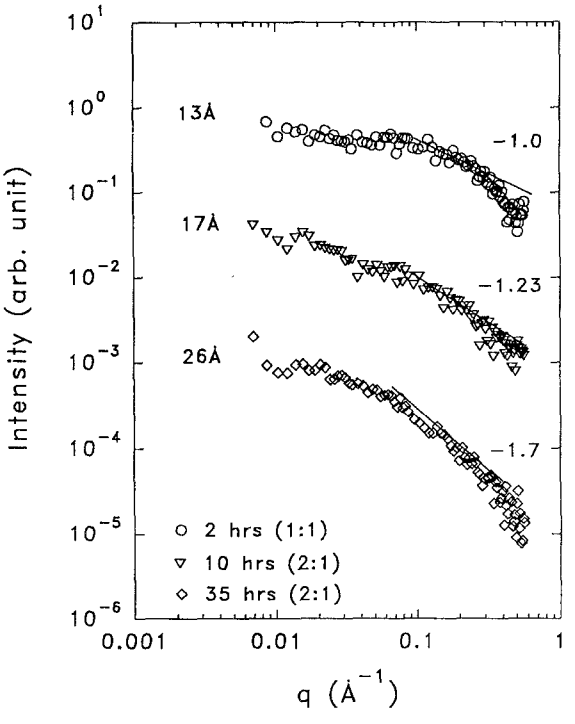

(a)

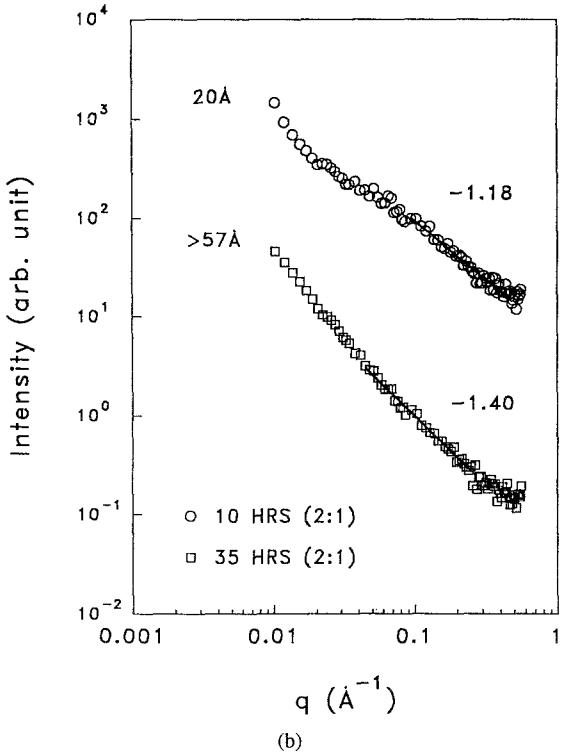

(b)

Fig. 8. Small angle x-ray scattering (SAXS) Porod plot for: (a) the A2(fresh) and (b) the A2(aged) sols after different aging times. Values presented on each scattering curve correspond to the Guinier radius (R_G) and Porod slope.

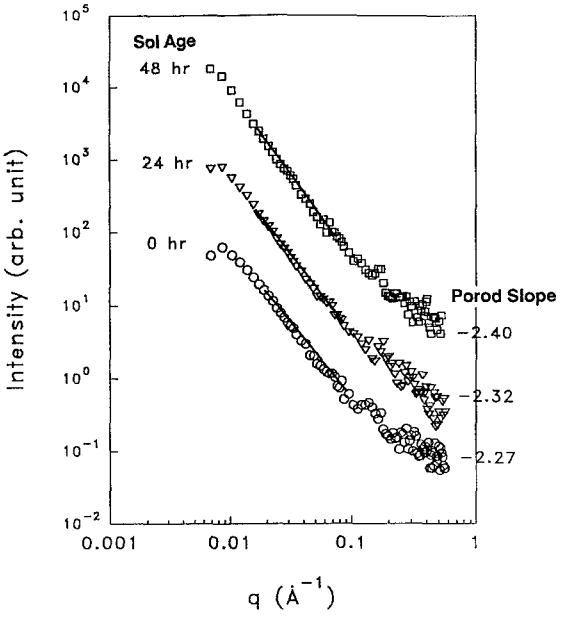

(a)

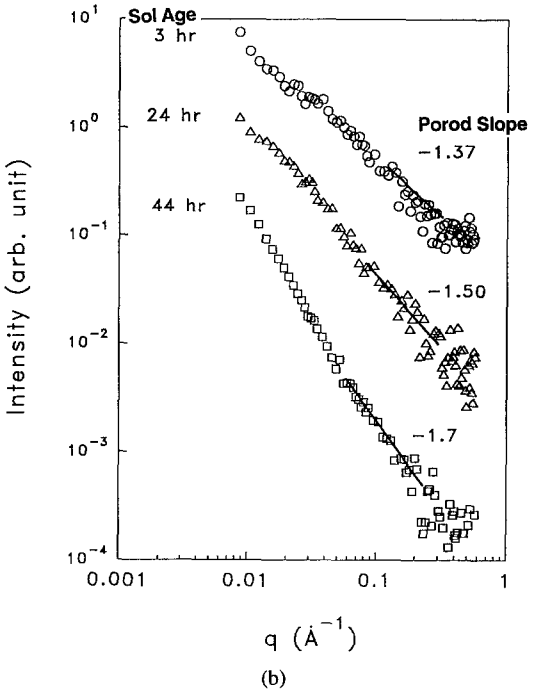

(b)

Fig. 9. SAXS Porod plots of: (a) B2 sols (diluted 5:1) after different periods of aging at 50°C, and AAB sols (diluted 5:1) after different periods of aging at room temperature. Values presented on the plot indicate the mass fractal dimensions.

dimers remains virtually constant with aging, the concentration of the singly hydrolyzed dimer (−86.5 ppm) decreases dramatically. The concomitant increase in the unhydrolyzed cyclic tetramer suggests the reaction

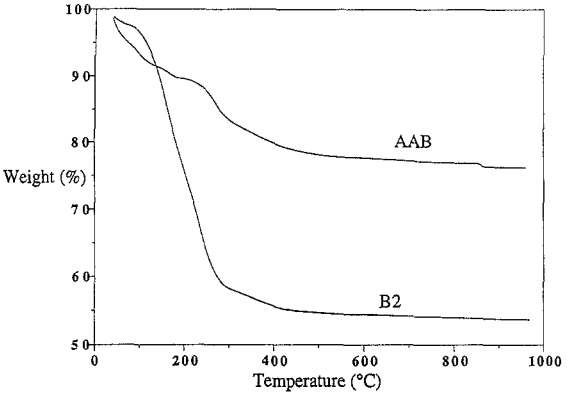

Fig. 10. TGA results for B2 and AAB dried gels heated at 2°C/min to 550°C and then 10°C/min to 1000°C in flowing air.

sequence: $2(RO)_5(HO)Si_2O \rightarrow (RO)_9(HO)Si_4O_3 \rightarrow (RO)_8Si_4O_4$. The preferential cyclization of the linear tetramer is a consequence of the steric bulk of the two pendant ethoxide groups per silicon, favoring cyclic over linear species, and the dearth of hydrolyzed sites, causing intramolecular condensation to be favored over intermolecular condensation.

4.2 A2 sols

A2 sols were prepared by acid-catalyzed hydrolysis of the fresh or aged stock solutions with excess water ($r = 5$). Comparisons made in Figs. 4 and 14 indicate that, after two hours of aging, the A2(fresh) sol is less highly condensed than the A2(aged) sol. However, with additional aging time, both the Q-distributions and extents of reaction of A2(fresh) and A2(aged) sols become comparable. Despite these similarities in the average molecular-scale structure, the SAXS results presented in Figs. 8(a) and (b) indicate that differences in the stock solution preparation significantly influence structure on intermediate length scales (0.2−10 nm). After comparable aging times, the A2(aged) sols are characterized by larger size, lower fractal dimension, and a wider range of fractal scaling behavior. The combined NMR and SAXS results are consistent with the greater incorporation of cyclic tetramers in siloxane polymers formed in the A2(aged) sols. Previous NMR studies have shown the cyclic tetramer and oligomers containing cyclic tetramer to be rather stable with respect to ring-opening hydrolysis or alcoholysis under acid-catalyzed conditions (9) or without added catalyst (12). These stiffer structural units, when incorporated into the siloxane

Table 1. Refractive index and thickness values determined by ellipsometry for films prepared from A2(fresh) and A2(aged) sols after various times of aging. Volume fraction porosities are calculated from the refractive index using the Lorentz-Lorenz model.

Aging at 50°C (t/t_{gel})	A2 sols from fresh stock solution			A2 sols from aged stock solution		
	Thickness (Å)	Refractive index	Vol. frac. porosity	Thickness (Å)	Refractive index	Vol. frac. porosity
0.05	1580	1.403	0.1	1376	1.398	0.1
0.24	1590	1.398	0.1	1359	1.415	0.08
0.82	2245	1.401	0.1	1369	1.409	0.09

Table 2. Refractive indices and vol% porosities (calculated from the Lorentz-Lorenz relation) for films dip-coated from B2 sols and AAB sols (diluted 5:1) as a function of aging time (or aging time normalized by the gelation time). Gelled samples were sonicated to a coatable consistency. Mass fractal dimension values are for sols aged for comparable normalized aging times (Fig. 9).

B2 Sol:			As-deposited:		After 400°C:	
Aging time (hr at 50°C)	Aging time (normalized)	D	Refractive index	Porosity (vol %)	Refractive index	Porosity (vol %)
0.0	0.00	2.27	1.425	4.9	1.369	16.0
24.0	0.32	2.32	1.424	5.0	1.346	20.8
48.0	0.63	2.40	1.421	5.6	1.325	25.1
72.0	0.95	–	1.418	6.2	1.292	32.1
94.0	1.24	–	1.417	6.4	1.240	43.5

AAB Sol:			As-deposited:		After 400°C:	
Aging time (hr at 23°C)	Aging time (normalized)	D	Refractive index	Porosity (vol %)	Refractive index	Porosity (vol %)
0.0	0.00	–	1.435	2.9	1.381	13.6
2.5	0.05	1.37	1.432	3.5	1.378	14.2
21.0	0.43	1.50	1.398	10.2	1.365	16.9
43.0	0.86	–	1.369	16.0	1.341	21.8
45.0	0.90	1.70	1.353	19.3	1.331	23.9

backbone, would favor more extended growth, so that after the same extent of reaction, polymers would exhibit larger size and lower mass fractal dimension, consistent with our experimental results. Unfortunately, the breadth of the Q^3 and Q^4 NMR resonances of the A2 sols prevents quantification of the cyclic tetramer concentration.

4.3 B2 and AAB sols

B2 sols were prepared by base-catalyzed hydrolysis of aged stock solution with excess water ($r = 3.7$). Comparing the NMR spectra of the stock solution and the unaged B2 sol (Figs. 2 and 5), we observe that the base-catalyzed hydrolysis step causes considerable condensation as is evident from the production of Q^4 species at the expense of Q^2 and Q^3 species. However, the concentrations of the unhydrolyzed dimer and unhydrolyzed Q^2 silicon species associated possibly with trimer remain largely unchanged, and the concentration of monomer has clearly increased. These results suggest that, as expected from both steric and inductive considerations, base-catalyzed hydrolysis promotes further hydrolysis and condensation of more highly hydrolyzed and condensed species, leaving unhydrolyzed and more weakly condensed species comparatively unreacted. The generation of monomer can be attributed to base-catalyzed siloxane bond hydrolysis or alcoholysis, leading to a redistribution of siloxane bonds according to reactions of the general

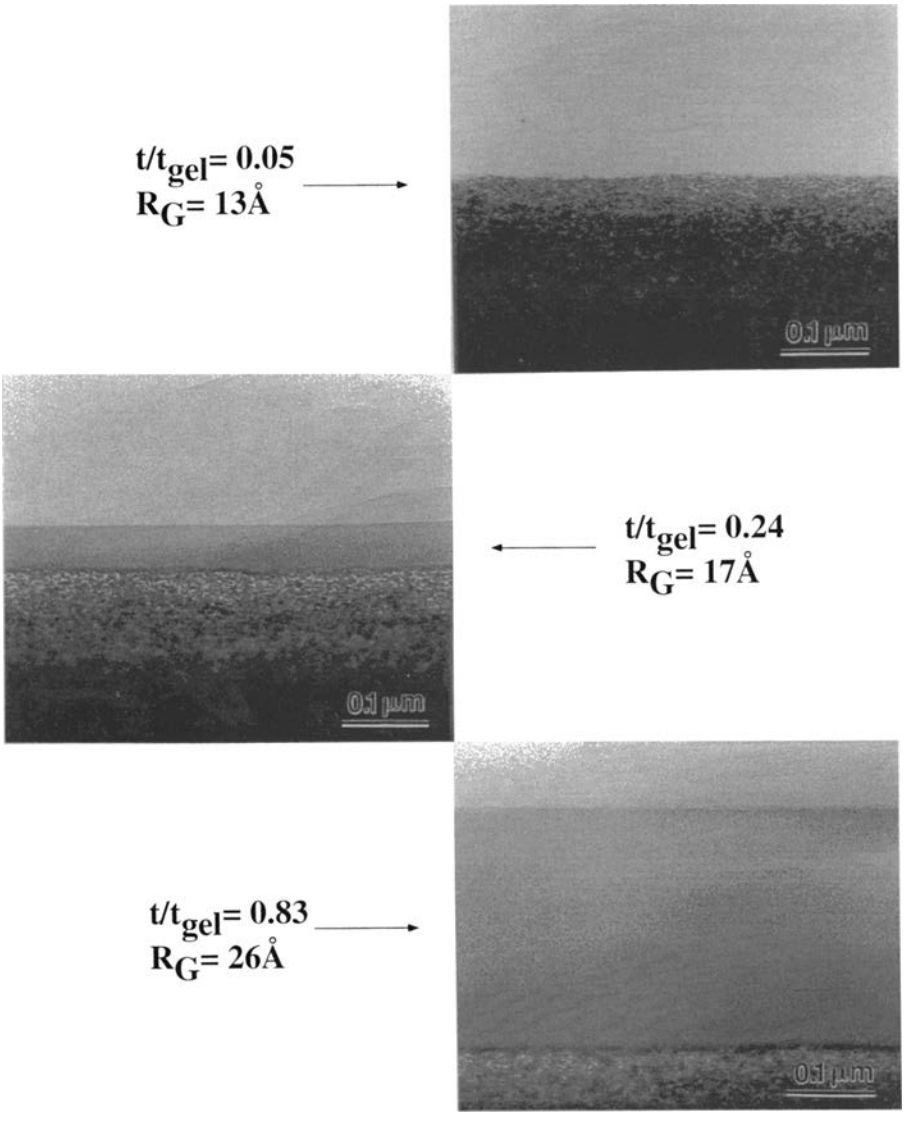

Fig. 11. Cross-sectional TEM micrographs of A2(aged) sols deposited on γ-Al_2O_3 supports after various sol aging times: (a) $t/t_{gel} = 0.05$ (b) $t/t_{gel} = 0.24$, and (c) $t/t_{gel} = 0.83$. EDS analysis (11) indicated that for $t/t_{gel} = 0.05$ silica deposition occurred exclusively within the pores of the γ-Al_2O_3 support.

type ($n \geq 2$):

$$\mathrm{ROH} + (\mathrm{RO})_{2n+2}\mathrm{Si}_n\mathrm{O}_{n-1} \leftrightarrow (\mathrm{RO})_4\mathrm{Si} + \mathrm{HO}(\mathrm{RO})_{2n-1}\mathrm{Si}_{n-1}\mathrm{O}_{n-2} \quad (5)$$

$$\mathrm{HO}(\mathrm{RO})_{2n-1}\mathrm{Si}_{n-1}\mathrm{O}_{n-2} + (\mathrm{RO})_{2n+2}\mathrm{Si}_n\mathrm{O}_{n-1} \leftrightarrow (\mathrm{RO})_{4n}\mathrm{Si}_{2n-1}\mathrm{O}_{2n-2} + \mathrm{ROH} \quad (6)$$

or

$$2\,\mathrm{Xmer} \leftrightarrow \mathrm{monomer} + (\mathrm{X}+1)\mathrm{mer} \quad (7)$$

where R = alkyl(siloxane bond alcoholysis) or H (siloxane bond hydrolysis). Both continued polymerization and siloxane bond hydrolysis or alcoholysis could account for the reduction in concentration of the cyclic tetramer Q^2_{4c} species with aging (Fig. 5). It is generally believed that siloxane bond hydrolysis is promoted under more basic conditions (13) consistent with our experimental results.

SAXS data for B2 sols show a general trend of increasing size and increasing mass fractal dimension with aging. These results are consistent with polymer growth accompanied by redistribution reactions. Continued cleavage of siloxane bonds to produce low

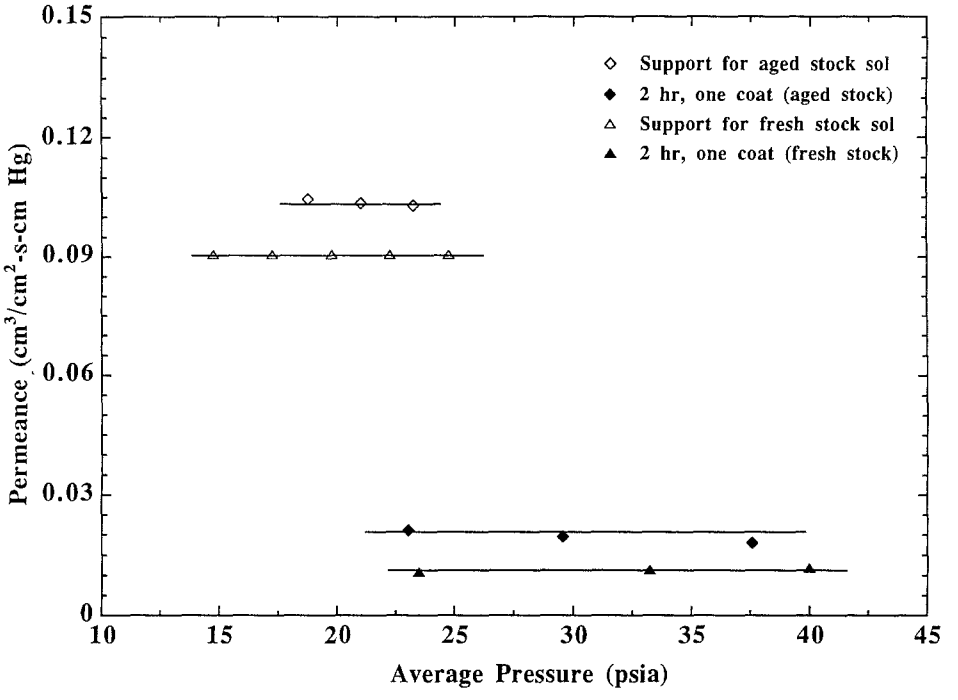

Fig. 12. Helium permeance data as a function for average pressure across the membrane of membranes from a single coating of A2(fresh) or A2(aged) sols after 2 hours of aging.

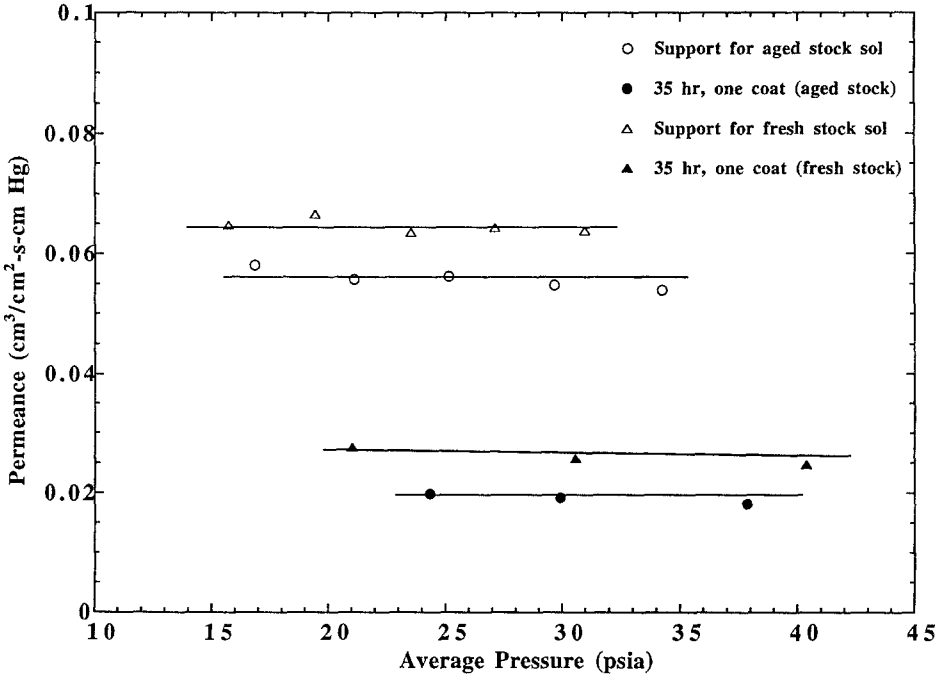

Fig. 13. Helium permeance data as a function of average pressure across the membrane for membranes prepared from a single coating of A2(fresh) or A2(aged) sols after 35 hours of aging.

Table 3(a). He permeance and reduction ratio for supports coated with A2(fresh) sols after different periods of aging followed by annealing at 400°C for 10 min. Reduction ratio is defined as the ratio of the permeance of the support to the permeance after one coat.

Permeance (cm^3/cm^2-s-cm Hg)—fresh stock solution			
A2 Sol Aging time (hr)	Support	After one coat	Reduction ratio
2	0.0906	0.0113	8.0
10	0.0617	0.0147	4.2
35	0.0646	0.0259	2.5

Table 3(b). He permeance and reduction ratio for supports coated with A2(aged) sols after different periods of aging followed by annealing at 400°C for 10 min. Reduction ratio is defined as the ratio of the permeance of the support to the permeance after one coat.

Permeance (cm^3/cm^2-s-cm Hg)—aged stock solution			
A2 Sol Aging time (hr)	Support	After one coat	Reduction ratio
2	0.1017	0.0196	5.2
10	0.0791	0.0135	5.8
35	0.0557	0.0190	2.9

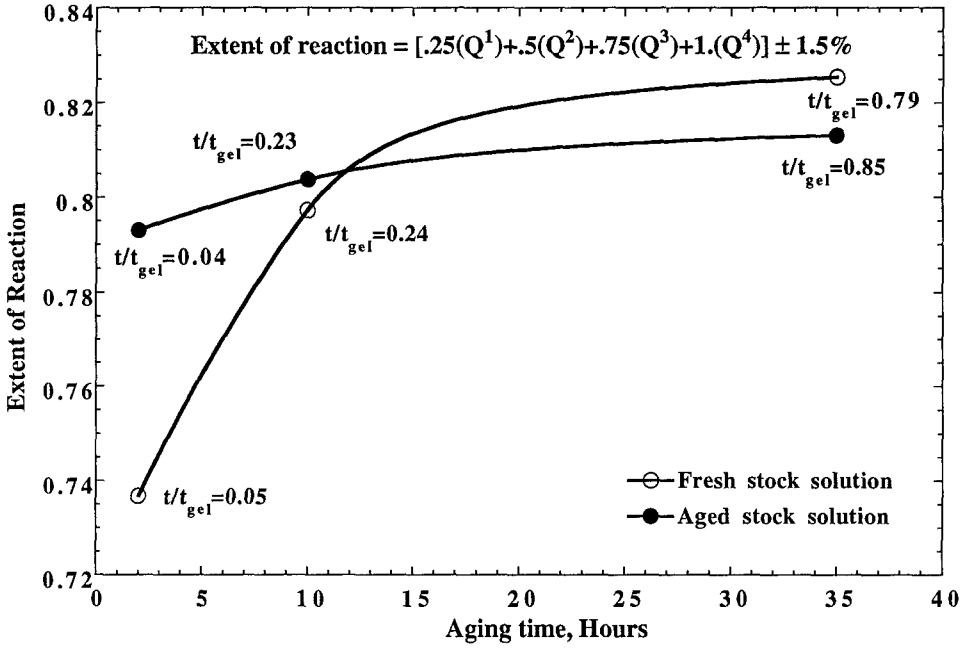

Fig. 14. Extent of reaction of the A2(fresh) and A2(aged) sols with aging time at 50°C.

molecular weight species followed by preferential re-condensation at more highly condensed sites is analogous to reaction-limited monomer-cluster growth or ripening, mechanisms which in time should lead to more compact, uniform structures characterized by $D \rightarrow 3$.

AAB sols were prepared by a three-step process involving acid-catalyzed hydrolysis of aged stock solution ($r = 2.5$) followed by a base-catalyzed hydrolysis step ($r = 3.7$). The final hydrolysis ratio, pH, and silicon concentration were identical to those of B2 sols. Comparing the NMR spectra of the stock solution and the AAB sol (Figs. 2 and 7), we see that the effect of the second (acid-catalyzed) hydrolysis step was to promote extensive hydrolysis and condensation. Monomer and Q^1 species were consumed to produce primarily a variety of Q^2 and Q^3 species. Various cyclic tetramers are prominent sol species after the second hydrolysis step as is evident from the strong Q^2 resonance observed near −95 ppm.

The third (base-catalyzed) hydrolysis step promotes further condensation of Q^2 and Q^3 species to produce primarily Q^3 and Q^4 species, and aging causes practically complete elimination of Q^2 species, including the cyclic tetramers (Fig. 7). These results are consistent with the conclusion drawn above: base additions are quite effective in catalyzing the hydrolysis and condensation of more highly-hydrolyzed and condensed species (products of the second hydrolysis step). The absence of monomer and dimer/Q^1 species implies that

monomer-producing redistribution reactions and siloxane bond cleavage reactions, in general, are inhibited for more highly condensed species. Overall, comparison of the NMR spectra of B2 and AAB sols proves that the hydrolysis and condensation pathways are strongly kinetically-limited for this composition.

The considerably lower mass fractal dimensions observed for AAB sols compared to B2 sols are consistent with the general expectation for reaction-limited cluster-cluster growth in the absence of monomers and oligomers (14). In addition, since cyclic tetramers are expected to promote the formation of extended polymers characterized by low values of the mass fractal dimension, the unusually low value of $D(1.4)$ observed after 3 hours of aging may be attributable to the incorporation of cyclic tetramers, formed during the second hydrolysis step, into the siloxane backbone. Progressive hydrolysis or alcoholysis of cyclic tetramers after the addition of base could partially account for the increase in D observed during aging. The absence of monomer and Q^1 species argues against ripening as being responsible for this behavior.

5 Discussion of film formation

This section examines the role of the molecular- and intermediate-scale structures of the sols in influencing the microstructure of the corresponding thin films formed by dipcoating. We consider the cases of mutually transparent and mutually opaque precursors.

5.1 Mutually transparent precursors

According to Eq. 3, we expect the conditions for mutual transparency to be fulfilled in general when $D < 1.5$. In addition, since Eq. 3 assumes an infinite condensation rate, mutual transparency may also be realized under conditions where D somewhat exceeds 1.5 if the condensation rate is low. The ellipsometry results obtained for both the A2(fresh) and A2(aged) series of sols show low volume percent porosities and essentially no dependence of porosity on sol age. These observations are completely consistent with the idea of mutual transparency: the ability of the polymers to freely interpenetrate as they are concentrated on the substrate surface should lead to dense packing and should effectively hide any differences due to size and fractal dimension of the individual primary species. For example, the differences noted in the scattering behavior of the A2(fresh) and A2(aged) sols are not manifested as differences in porosity in the ellipsometry data (Table 1).

The permeance data reported in Tables 3(a) and (b) also show similar trends for both A2(fresh) and A2(aged) sols. Sol deposition causes a significant reduction in the permeance of the support, and the reduction ratios are greatest after two hours of aging and decrease with aging time. This behavior may be explained by consideration of factors governing flow through a porous medium. The molar flux due to Knudsen flow through the membrane plus support layer can be described by:

$$J_K = \frac{4\varepsilon r_p}{3\tau RT}\left[\frac{2RT}{\pi M}\right]^{1/2}\frac{\Delta P}{\Delta a}, \qquad (8)$$

where ε is the porosity, τ is tortuosity, r_p is the pore radius, M is molecular weight, R is the gas constant, T is the temperature, ΔP is the partial pressure across the membrane or layer, and Δa is the membrane or layer thickness (15). Based on this expression the general reduction in permeance observed after membrane deposition is attributable to a decrease in porosity and/or pore size and an increase in tortuosity and/or thickness, consistent with the following observations:

(1) The ellipsometry data indicates that the membrane layer should have a porosity of about 10 vol% compared to the 30–40 vol% of the support layer.

(2) Cross-sectional TEM images of the support plus membrane (Fig. 11) suggest that the pore radius of the membrane layer is considerably smaller than that of the support (~2 nm).

(3) It is expected, and modeling has shown, that the permeation tortuosity of a material will become large and strongly dependent on porosity for volume fraction porosities near the percolation threshold (~16%) (16).

The combined features of low porosity, small pore size, and large tortuosity attributable to all the (A2) membranes studied are responsible for the large reductions in permeance observed after membrane deposition.

The general trend of decreasing reduction ratios with increasing aging times can be explained by consideration of the relative sizes of the precursor species and the pores of the γ-Al_2O_3 support layer. Combined cross-sectional TEM and SAXS results (Figs. 11 and 8) indicate that when the characteristic polymer size R_G is appreciably less than the pore radius of the support, ~2 nm, deposition of silica occurs primarily within the ~4 μm thick support layer (as confirmed by EDS analysis (11)), whereas when $R_G \geq 2$ nm, an external

membrane layer is formed on the support surface. For the same quantity of silica deposition, penetration into the support pores causes the effective thickness to be greater than when the membrane is formed as an external layer. (Since the support has a volume fraction porosity of about 33%, the depth of penetration into the support must be a factor of about 3 larger than the thickness of an external film for equivalent quantities of deposited silica). According to Eq. 8, greater film thickness results in reduced flux and correspondingly larger reduction ratios. The series of TEM micrographs shown in Fig. 11 (a–c) indicate that with increased aging (increased R_G) silica is more efficiently filtered-out by the support to form an external membrane layer. This should cause a progressive decrease in overall membrane thickness (internal plus external layer thicknesses) with aging time, explaining the observed trend. For the series of sols studied, there is no evidence that the porosity, tortuosity, or pore size of the deposited films or membranes depend on the pedigree of the stock solution or sol aging times.

5.2 *Mutually opaque precursors*

Based on Eq. 3, B2 sols fulfill the criterion for mutual opacity ($D > 1.5$), so we expect film porosity to increase with size of the primary sol species (Eq. 2). Although both NMR and SAXS data are consistent with polymer growth during aging, the as-deposited (unannealed) films showed essentially no dependence of refractive index on aging time (Table 2). The expected reduction in refractive index with sol aging time was observed only after heating to 400°C. These results are explained by the presence of unreactive monomers and oligomers in the B2 sols. ^{29}Si NMR (Fig. 5) shows evidence for several unhydrolyzed or weakly hydrolyzed monomers and oligomers (especially dimer) in the B2 sols regardless of aging time. The presence of these small species should not influence the SAXS results performed under rather dilute conditions. However, as the sol is concentrated during film deposition, these small weakly reactive species will freely penetrate the larger fractal clusters, "filling-in" the cluster porosity. The heat treatment at 400°C pyrolyzes the residual alkoxide groups associated primarily with these small species revealing the trend of increasing porosity with increasing cluster size expected for mutually opaque precursors.

Compared to B2 sols, AAB sols exhibit larger polymer sizes, lower mass fractal dimensions, and no evidence for monomers or oligomers after aging for equivalent normalized times. Mass fractal dimensions increase from 1.4 to 1.7 with aging time, so we expect a transition from mutually transparent to mutually opaque behavior. Refractive index values of the as-deposited films (Table 2) are consistent with this expectation. Films prepared from unaged AAB sols are quite dense. Porosity increases monotonically with aging time due to increased size and mass fractal dimension of the primary sol species. Increased size increases the porosity of a fractal object according to Eq. 2. Increased mass fractal dimension reduces the porosity of an individual object but reduces the probability of interpenetration (Eq. 3), which, in the absence of monomer and oligomers, allows the porosity of the primary species to be partially preserved in the as-deposited films. *In order to maximize film porosity, it is necessary to avoid small unreactive species and to chose an intermediate value of D that balances the effects of the primary cluster porosity and the secondary aggregate porosity.*

As shown in Table 2, heating to 400°C causes an increase of about 6% in film porosity attributable to organic removal. The porosity created by pyrolysis of AAB films is considerably less than that created in B2 films consistent with TGA results (Fig. 10), which show about a factor of three difference in weight loss in the temperature range 150–400°C. After heating, a similar trend of increasing porosity with increasing aging time is observed. It should be emphasized that this behavior and that of B2 sols is completely different from the behavior of the A2 series of sols where no effect of sol aging time on film porosity is observed after heating to 400°C. It is this distinction that provides a working definition of the concept of mutual transparency and mutual opacity in the context of film formation and that allows the rational design of thin film precursors.

Comparing the results of the A2 and AAB series of films, we observe what appears to be conflicting behavior, viz. A2 sols exhibiting $D = 1.7$ (Fig. 8a) yield rather dense films consistent with mutual transparency, whereas AAB sols exhibiting $D = 1.7$ (Fig. 9b) yield porous films consistent with mutual opacity. This apparent inconsistency is explained by the assumptions underlying Eq. 3 that condensation occurs immediately and irreversibly at each point of intersection and that the individual aggregating units are perfectly stiff. A2 sols exhibit lower condensation rates than AAB sols and are somewhat less-highly condensed. Thus although D exceeds 1.5 for the A2 sol, its behavior is consistent with mutual transparency. The AAB sol better fulfills

the assumptions of the model, and the films exhibit behavior consistent with the model predictions.

6 Summary

This study provides several examples of how, using multi-step hydrolysis procedures, the sequence (acid-acid, acid-base, acid-acid-base) and timing of the successive steps influences the molecular and intermediate-scale structure of silica sols prepared from alkoxide precursors. These examples imply that the silica polymerization pathway is largely kinetically controlled at least for moderate values of r.

Under acid-catalyzed conditions with molar hydrolys is ratios $r = 1$ or 2.5, aging (at 0°C, room temperature, or under reflux) served to increase the concentration of cyclic tetrasiloxanes, which in turn influenced the intermediate-scale structure of polymers formed during subsequent acid- or base-catalyzed hydrolysis. Presumably incorporation of structurally rigid cyclic tetramers into the siloxane backbone leads to more extended structures characterized by larger size and lower mass fractal dimension.

It was shown that the species distribution resulting from base-catalyzed hydrolysis depends strongly on the extent of hydrolysis and condensation of the precursor sol to which the base is added. Base additions, when made to a pre-hydrolyzed sol, serve to catalyze condensation of more highly hydrolyzed and condensed species, leaving weakly hydrolyzed monomers and oligomers virtually unreacted. Even after long periods of aging, the species distribution identified by NMR differed profoundly for two sols prepared with the same value of r, pH, and concentration, but with a different sequence of steps.

With regard to thin film formation, we defined two classes of primary sol species referred to as mutually transparent or mutually opaque. Mutually transparent species are able to interpenetrate during dip-coating to produce rather dense films that exhibit no dependence of refractive index/porosity on polymer size or mass fractal dimension. Mutually opaque species do not freely interpenetrate during dip-coating. In the absence of monomer or oligomeric species that are able to fill-in small pores, we observe a systematic increase in film porosity with aging time attributable to increasing size and mass fractal dimension of the primary species. The ability to "tune" the refractive index by a simple aging procedure should allow the rational design of porous films.

Acknowledgments

Part of this work was performed at Sandia National Laboratories, supported by the U.S. Department of Energy Basic Energy Sciences Program under Contract #DE-AC04-94AL85000. Additional support has been received from the National Science Foundation (Contract #CTS9101659), the Electric Power Research Institute (Contract #RP8007-15), the Gas Research Institute (Contract #5091-222-2306), and the Morgantown Energy Technology Center. The authors thank D.C. Goodnow for the TGA results.

References

1. C.J. Brinker, A.J. Hurd, P.R. Schunk, G.C. Frye, and C.S. Ashley, J. Non-Cryst. Solids, **147&148**, 424 (1992).
2. B.B. Mandelbrot, *The Fractal Geometry of Nature* (W.H. Freeman, New York, 1983).
3. C.J. Brinker, K.D. Keefer, D.W. Schaefer, R.A. Assink, B.D. Kay, and C.S. Ashley, J. Non-Cryst. Solids, **63**, 45 (1984).
4. D.L. Logan, C.S. Ashley, and C.J. Brinker in *Better Ceramics through Chemistry V*, edited by M.J. Hampden-Smith, W.G. Klemperer, and C.J. Brinker (Materials Research Society, Pittsburgh, 1992), **271**, p. 541.
5. D.L. Logan, C.S. Ashley, R.A. Assink, and C.J. Brinker in *Sol-Gel Optics II*, edited by J.D. Mackenzie (SPIE—The International Society of Optical Engineering, Bellingham, WA, 1992), **1758**, p. 519.
6. R.A. Assink and B.D. Kay, Annu. Rev. Mater. Sci., **21**, 491 (1991).
7. C.J. Brinker, T.L. Ward, R. Sehgal, N.K. Raman, S.L. Hietala, D.M. Smith, D.-W. Hua, and T.J. Headley, J. Membrane Science, **77**, 165 (1993).
8. V.G. Engelhardt, W. Altenburg, D. Hoebbel, and W.Z. Weiker, Anorg. Allg. Chem., **418**, 43 (1977).
9. L.W. Kelts, N.J. Effinger, and S.M. Melpolder, J. Non-Cryst. Solids, **83**, 353 (1986).
10. C.A. Balfe and S.L. Martinez in *Better Ceramics Through Chemistry II*, edited by C.J. Brinker, D.E. Clark, and D.R. Ulrich (Materials Research Society, Pittsburgh, 1986), **73**, p. 27.
11. C.J. Brinker, R. Sehgal, N.K. Raman, P.R. Schunk, and T.J. Headley, J. Sol-Gel Sci. & Tech., in Press.
12. W.G. Klemperer, V.V. Mainz, and D.M. Millar in *Better Ceramics Through Chemistry II*, edited by C.J. Brinker, D.E. Clark, and D.R. Ulrich (Materials Research Society, Pittsburgh, 1986), **73**, p. 3.
13. C.J. Brinker and G.W. Scherer, *Sol-Gel Science: The Physics and Chemistry of Sol-Gel Processing* (Academic Press, San Diego, 1990), p. 214.
14. C.J. Brinker and G.W. Scherer, *Sol-Gel Science: The Physics and Chemistry of Sol-Gel Processing* (Academic Press, San Diego, 1990), p. 194.
15. K. Keizer, R.J.R. Uhlhorn, R.J. Van Vuren, and A.J. Burggraaf, J. Membrane Science, **39**, 285 (1988).
16. R. Zellen, *The Physics of Amorphous Solids* (John Wiley and Sons, New York, 1983), p. 183.